Polarization-independent absorption enhancement in a graphene square array with a cascaded grating structure

Jun Wu*

Shanghai Institute of Optics and Fine Mechanics, Chinese Academy of Sciences, No. 390 Qinghe Road, Jiading District/ PO Box 800-211, Shanghai, People's Republic of China. *Correspondence e-mail: mailswj2011@163.com

The polarization-independent enhanced absorption effect of graphene in the near-infrared range is investigated. This is achieved by placing a graphene square array on top of a dielectric square array backed by a two-dimensional multilayer grating. Total optical absorption in graphene can be attributed to critical coupling, which is achieved through the combined effect of guided-mode resonance with the dielectric square array and the photonic band gap with the two-dimensional multilayer grating. To reveal the physical origin of such a phenomenon, the electromagnetic field distributions for both polarizations are illustrated. The designed graphene absorber exhibits near-unity polarization-independent absorption at resonance with an ultra-narrow spectrum. Moreover, the polarization-independent absorption can be tuned simply by changing the geometric parameters. The results may have promising potential for the design of graphene-based optoelectronic devices.

1. Introduction

As a one-atom-thick two-dimensional carbon material, graphene has spurred huge research interest owing to its unique electrical, optical and thermal properties (Bonaccorso *et al.*, 2010; Grigorenko *et al.*, 2012; Bao & Loh, 2012). Since it was first produced in 2004 (Novoselov *et al.*, 2004), it has already been applied in optoelectronic and plasmonic devices, exploiting features such as plasmonically induced transparency (Cheng, Chen, Yu, Duan *et al.*, 2013), absorption (Thongrattanasiri *et al.*, 2012; Alaee *et al.*, 2012; Wang *et al.*, 2017; Yang, Wang *et al.*, 2016), photodetection (Xia *et al.*, 2009), optical modulation (Liu *et al.*, 2016), imaging (Sensale-Rodriguez *et al.*, 2013), plasmon waveguiding (Christensen *et al.*, 2012; Lu *et al.*, 2017), optical forces (Yang, Shi *et al.*, 2016), biosensing (Wei *et al.*, 2015; Wu *et al.*, 2016), and polarization encoding and conversion (Cheng, Chen, Yu, Li, Deng & Tian, 2013; Cheng, Chen, Yu, Li, Xie *et al.*, 2013; Li *et al.*, 2016). For applications in photodetectors (Zhang *et al.*, 2013) and absorbers/thermal emitters (Thongrattanasiri *et al.*, 2012; Alaee *et al.*, 2012; Wang *et al.*, 2017; Yang, Wang *et al.*, 2016), strong absorption is highly desirable, so absorption enhancement in graphene has recently been a rapidly developing field.

In the long-wavelength regions (mid- to far-infrared ranges), graphene has two crucial characteristics. One is that its optical properties can be tuned using chemical or electrostatic gatings (Mark *et al.*, 2008), which indicates that the plasmon frequency of graphene can be controlled by the Fermi energy or chemical potential. The other is that graphene can support a strong plasmonic response in these regions, which can be employed to create a strong light–graphene interaction platform (Christensen *et al.*, 2012; Koppens *et al.*,

research papers
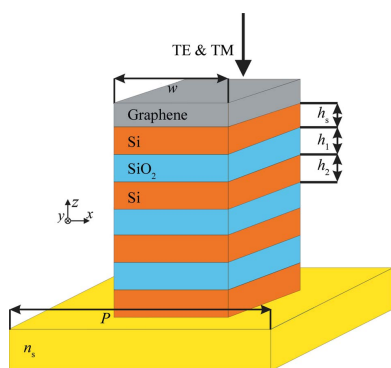
2011). Based on this strong plasmonic resonance, some graphene absorbers with total absorption have been proposed, such as periodic arrays of doped graphene nanodiscs (Thongrattanasiri *et al.*, 2012) and graphene micro-ribbon metamaterials (Alaee *et al.*, 2012). In contrast, in the visible and near-infrared ranges ($\lambda < 2\,\mu m$), undoped graphene does not support a plasmonic response (Xia *et al.*, 2013) and has only a wavelength-independent absorption of about 2.3% for a graphene monolayer with light at normal incidence (Nair *et al.*, 2008). Various methods have been proposed to enhance absorption in these frequency ranges, such as the combination of a graphene monolayer with metal nanostructures (Cai *et al.*, 2015), a simple one-dimensional dielectric grating based on the guided-mode resonance effect (Grande *et al.*, 2014), and graphene strips with a multilayer subwavelength grating based on the critical coupling effect (Hu *et al.*, 2014). However, the absorbers proposed above are all polarization-sensitive. To solve this problem, two-dimensional periodic structures should be employed. Liu and co-workers proposed the use of a one-dimensional photonic crystal with polarization-insensitive absorption, but the enhancement ratio is very small (Liu *et al.*, 2012). Piper and co-workers demonstrated that total absorption can be achieved in a graphene monolayer with a photonic crystal resonator by means of critical coupling (Piper & Fan, 2014). Furthermore, they demonstrated that total absorption can be achieved by degenerate critical coupling (Piper *et al.*, 2014).

In this work, the polarization-independent total absorption in graphene at normal incidence for near-infrared frequencies is investigated. A graphene absorber, which consists of a graphene square array on top of a dielectric square array backed by a two-dimensional multilayer grating, is designed and studied. The rigorous coupled-wave analysis (RCWA) (Li, 1997) is employed to obtain the optimized structure parameters and numerical results of the optical performance, which are also confirmed by the coupled-mode theory (Piper & Fan, 2014). The effect of the structure parameters on the absorption spectrum is also investigated. Furthermore, the electromagnetic field distributions for both polarizations are illustrated to give a physical understanding of such phenomena.

2. Design and analysis of the graphene absorber

The unit geometry of the proposed graphene absorber is depicted in Fig. 1. It consists of a graphene square array on top of a dielectric square array backed by a two-dimensional multilayer grating, which is supported by a substrate with refractive index n_s. The material of the dielectric square array is Si with a refractive index of 3.48. It has a width w and thickness h_s. The two-dimensional multilayer grating is composed of a three-period SiO$_2$/Si grating layer with refractive indexes of 1.45 and 3.48, respectively. Their corresponding thicknesses are h_1 and h_2, respectively. The period of the unit is P and the width is w. Transverse electric (TE) polarization (electric field parallel to the y axis) and transverse magnetic (TM) polarization (magnetic field parallel to the y axis) monochromatic plane waves are incident from air at an angle θ.

The optical properties of graphene in the near-infrared region are described by its complex refractive index n, which is derived as follows (Bruna & Borini, 2009),

$$n = 3.0 + \frac{iC_1\lambda_0}{3}, \tag{1}$$

where the constant $C_1 \simeq 5.446\,\mu m^{-1}$ and λ_0 is the operating wavelength.

After some numerical effort based on the RCWA, the optimized structure parameters with an operating wavelength of 1540 nm are obtained as follows: $P = 1270$ nm, $w = 755$ nm, $h_s = 315$ nm, $h_1 = 325$ nm, $h_2 = 340$ nm and $n_s = 1$. In Fig. 2, we plot the absorption spectrum at normal incidence for the designed graphene absorber. As can be seen from the figure,
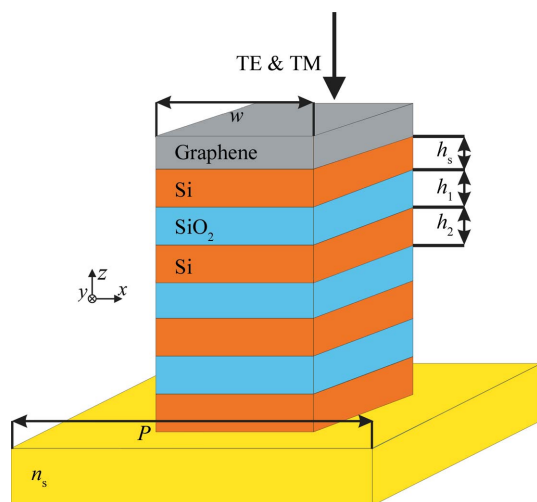
Figure 1
The configuration of the absorber, consisting of a graphene square array resting on a silicon square array backed by a two-dimensional multilayer grating. P is the period of the square array, w is the side width, h_s is the thickness of the Si square array, and h_1 and h_2 are the thicknesses of the SiO$_2$ and Si layers, respectively.
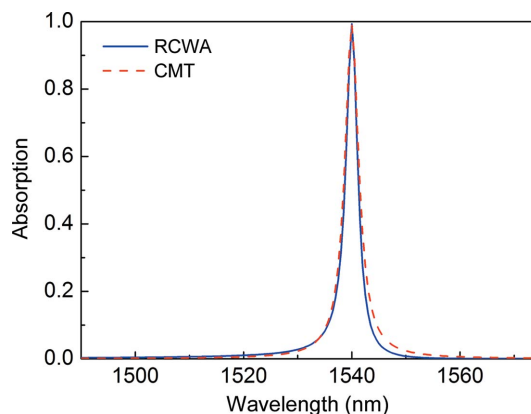
Figure 2
Comparison of absorption spectra calculated by RCWA and the CMT model for the graphene absorber with an operating wavelength of about 1540 nm.

a polarization-independent absorption of about 99.28% is achieved at a wavelength of 1540 nm. Moreover, the absorption has an ultra-narrow spectrum profile with a full width at half-maximum (FWHM) of only 2.5 nm.

To reveal the physical principles behind such a total-absorption phenomenon, the coupled-mode theory (CMT) is employed (Piper & Fan, 2014). We consider the absorber as a resonator. At the resonant frequency ω_0 it has a resonant amplitude of a. In the presence of material loss, the coupled-mode equations of the resonator can be described by (Piper & Fan, 2014)

$$\frac{\mathrm{d}a}{\mathrm{d}t} = (j\omega_0 - \gamma_\mathrm{e} - \delta)\, a + (2\gamma_\mathrm{e})^{1/2} y_\mathrm{in}, \qquad (2)$$

$$y_\mathrm{out} = (2\gamma_\mathrm{e})^{1/2} a - y_\mathrm{in}, \qquad (3)$$

where y_in and y_out are the amplitudes of the input and output waves, respectively, and γ_e and δ are the external leakage rate and intrinsic loss rate, respectively, which are extracted from the numerical simulation. With these parameters, the absorption can be described by (Piper & Fan, 2014)

$$A = \frac{4\delta\gamma_\mathrm{e}}{(\omega - \omega_0)^2 + (\delta + \gamma_\mathrm{e})^2}. \qquad (4)$$

From the above equation, we can see that, at resonance ($\omega = \omega_0$), complete absorption can be achieved when the external leakage rate and the intrinsic loss rate are the same ($\gamma_\mathrm{e} = \delta$); this effect is referred to as critical coupling (Xia *et al.*, 2013). A detailed review of the CMT is given by Piper & Fan (2014).

The theoretical absorption spectrum from the coupled-mode equation (4) is also shown in Fig. 2. The absorption spectrum calculated by RCWA is commendably consistent with the result from the CMT model for frequencies around resonance. However, a small deviation between them will occur for wavelengths away from resonance. This indicates that the CMT can give a good understanding of the critical coupling effect employed in this work.

In order to understand such perfect absorption intuitively, the distributions of electric and magnetic field intensity under normal incidence at the resonant wavelength were investigated. The electromagnetic field distributions for TE polarization are shown in Fig. 3, while those for TM polarization are shown in Fig. 4. As can be seen from Fig. 3(*a*), there is a large electric intensity enhancement and concentration at the top and bottom interfaces of the silicon square array, which leads to a large electric field intensity enhance-

ment in the graphene plane, as clearly illustrated in Fig. 3(*b*). In general, the absorption of energy arises from the power loss in a device. Further, for nonmagnetic materials, the time-averaged power loss density is given by (Hao *et al.*, 2011; Chern & Hong, 2011):

$$\frac{\mathrm{d}P_\mathrm{loss}}{\mathrm{d}V} = \frac{1}{2}\varepsilon_0\omega\,\mathrm{Im}(\varepsilon)\,|E|^2, \qquad (5)$$

where ε_0 is the permittivity of a vacuum, ω is the angular frequency, $\mathrm{Im}(\varepsilon)$ denotes the imaginary part of the relative permittivity and E denotes the electric field. A large $\mathrm{Im}(\varepsilon)$ and a strong electric field intensity should be employed to enhance absorption in a system. Therefore, a strong electric field intensity enhancement in the graphene plane can considerably increase the absorption in graphene. The magnetic field distribution of $|H_x|^2$ shows a strong magnetic field intensity enhancement at the centre of the silicon square array, whereas it is large at the four corners of the silicon square array for $|H_z|^2$.

Analysis of the TM polarization is similar to that of the TE polarization only with a different electromagnetic field component, as depicted in Fig. 4. The electric field intensity distribution of $|E_x|^2$ in the $y = 0$ plane shows a strong electric field intensity enhancement at the top and bottom interfaces of the silicon square array, which results in a large electric field intensity enhancement in the graphene plane for the $|E_x|^2$
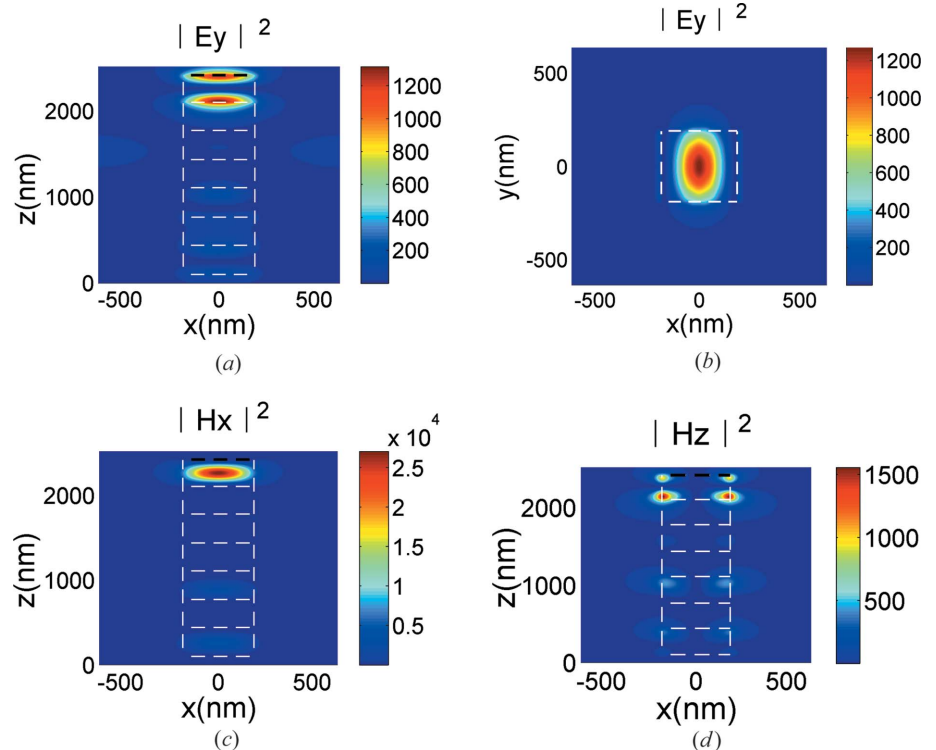
Figure 3
Electromagnetic field intensity distributions for TE polarization. (*a*) $|E_y|^2$ in the $y = 0$ plane (*xz* plane), (*b*) $|E_y|^2$ in the graphene plane, (*c*) $|H_x|^2$ in the $y = 0$ plane and (*d*) $|H_z|^2$ in the $y = 0$ plane. In panel (*b*), the region enclosed by the white dashed line is the graphene square array. In panels (*a*), (*c*) and (*d*), the regions denoted by white dashed lines are the silicon square array and the two-dimensional multilayer grating, while the black dashed lines indicate the graphene square array owing to its ultrathin nature.
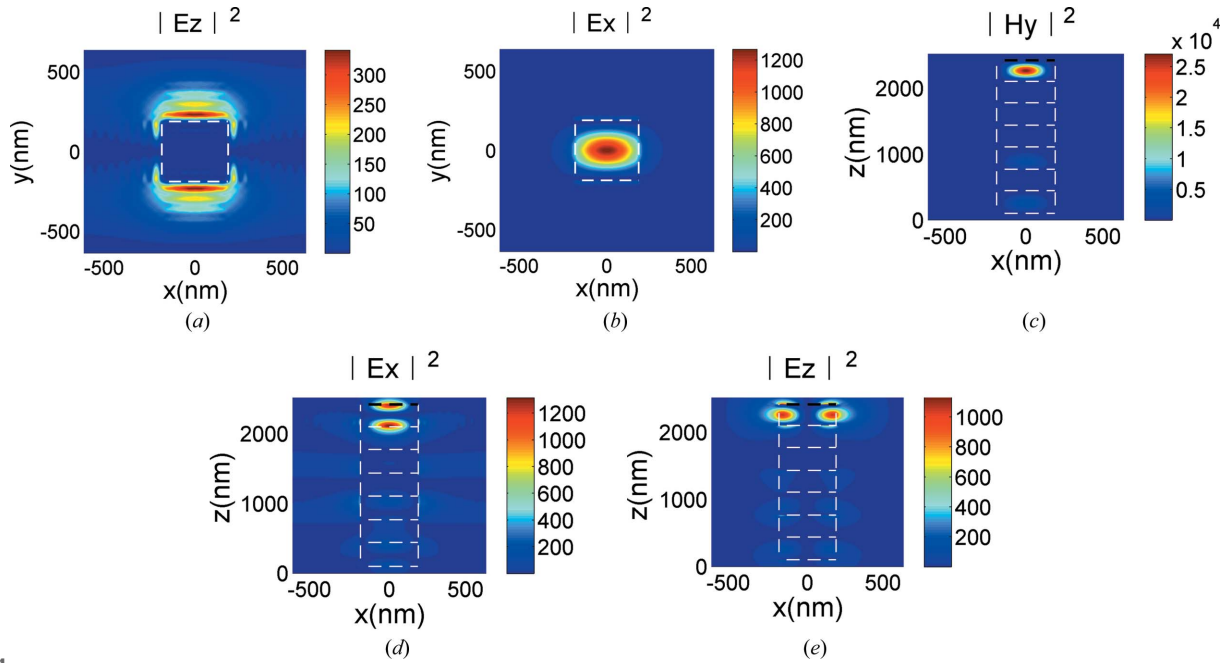
Figure 4
Electromagnetic field intensity distributions for TM polarization. (a) $|E_z|^2$ in the graphene plane, (b) $|E_x|^2$ in the graphene plane, (c) $|H_y|^2$ in the $y = 0$ plane (xz plane), (d) $|E_x|^2$ in the $y = 0$ plane and (e) $|E_z|^2$ in the $y = 0$ plane. In panels (a) and (b), the region enclosed by the white dashed line is the graphene square array. In panels (c)–(e), the regions denoted by the white dashed lines are the silicon square array and the two-dimensional multilayer grating, while the black dashed lines indicate the graphene square array due to its ultrathin nature.
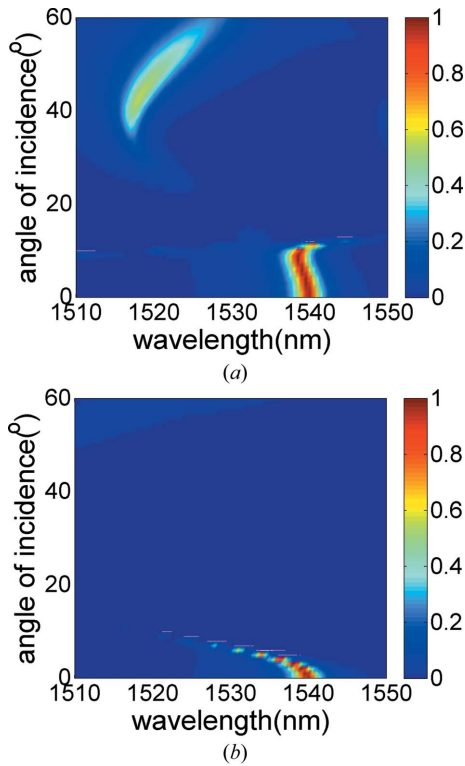
Figure 5
Absorption as a function of incident angle and wavelength for (a) TE and (b) TM polarization.

square array for $|E_z|^2$ in the graphene plane. Therefore, this electric field component has almost no contribution to the enhancement of absorption in graphene. Since the total electric intensity enhancement is the sum of the $|E_x|^2$ component and the $|E_z|^2$ component, the strong electric intensity enhancement of $|E_x|^2$ can still result in perfect absorption in graphene. The magnetic field distribution of $|H_y|^2$ shows a strong magnetic field intensity enhancement at the centre of the silicon square array. In general, the enhanced absorption in graphene for both polarizations can be attributed to critical coupling, which is realised by a combination of the guided-mode resonance effect in the silicon square array and the band-gap effect of the two-dimensional multilayer grating.

To investigate the angular sensitivity of the graphene absorber, the absorption as functions of both angle of incidence and wavelength for both polarizations are shown in Fig. 5. As can be seen, polarization-independent absorption disappears for incident angles departing from normal incidence. Moreover, it is noted that there is almost no absorption when the incident angle is above a value for TM polarization. The absorption is sensitive to the incident angle for both polarizations, which can be employed to tune the narrow-band absorption performance and used as a highly directed thermal emitter.

3. Discussion

The critical coupling can be controlled by adjusting the period P and width w of the unit. In Figs. 6(a) and 6(b), we show the absorption spectra for different P and w, respectively. The other structure parameters remain unchanged. It can be seen

component. The distribution of $|E_z|^2$ in the $y = 0$ plane shows a strong electric field intensity enhancement at the right and left interfaces of the silicon square array, and the electric field intensity enhancement is only large outside the graphene
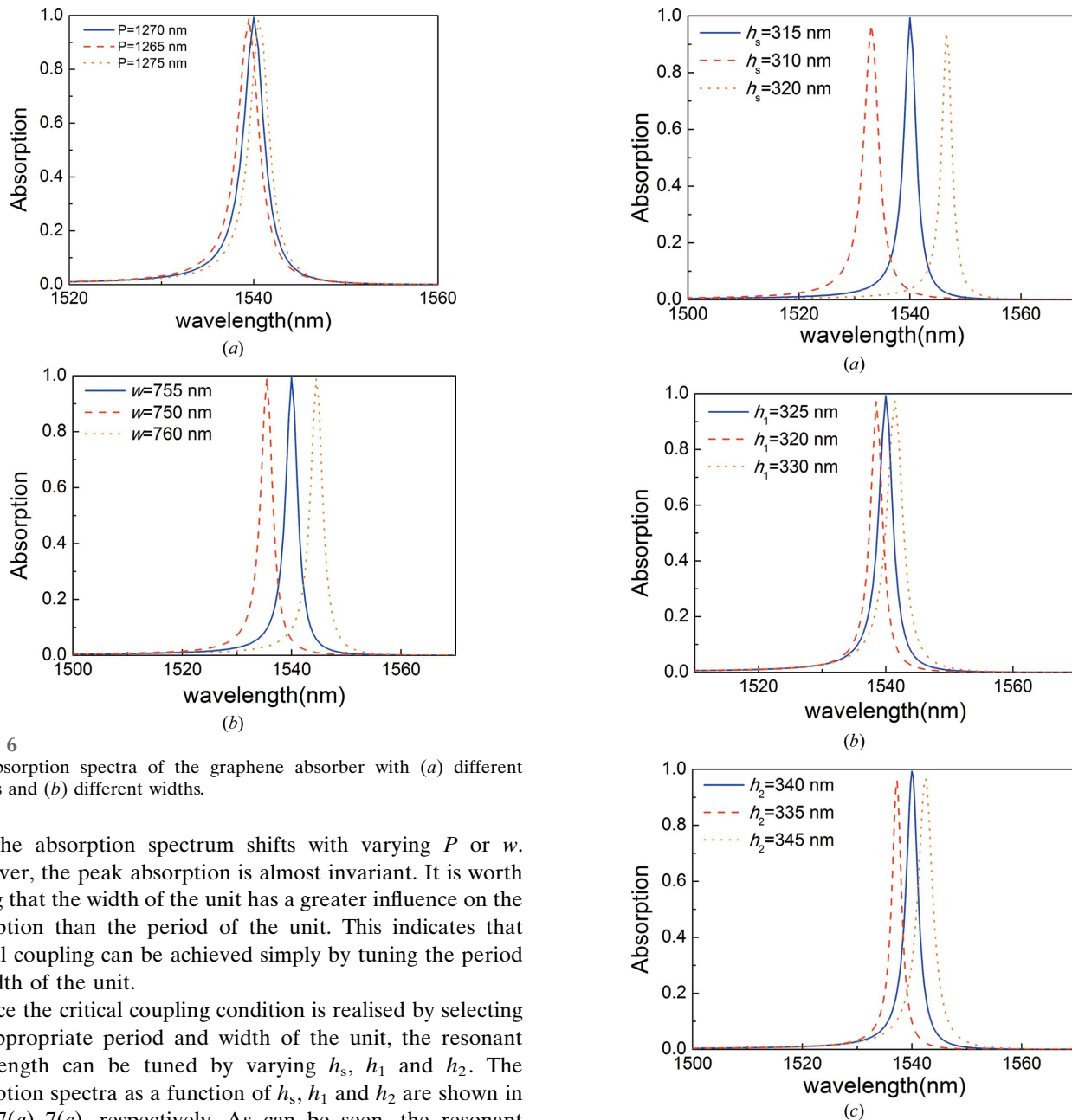
Figure 6
The absorption spectra of the graphene absorber with (*a*) different periods and (*b*) different widths.

that the absorption spectrum shifts with varying P or w. However, the peak absorption is almost invariant. It is worth noting that the width of the unit has a greater influence on the absorption than the period of the unit. This indicates that critical coupling can be achieved simply by tuning the period or width of the unit.

Once the critical coupling condition is realised by selecting the appropriate period and width of the unit, the resonant wavelength can be tuned by varying h_s, h_1 and h_2. The absorption spectra as a function of h_s, h_1 and h_2 are shown in Figs. 7(*a*)–7(*c*), respectively. As can be seen, the resonant wavelength increases with the thickness of the silicon square array, which shows a red shift. A similar phenomenon is observed for the variation in thickness of the periodic Si/SiO$_2$ grating layer. However, h_s has a greater influence on the absorption than h_1 or h_2. It is also worth noting that the peak absorption reduces slightly when the thickness deviates from the optimized values. This indicates a deviation from the coupling condition with a change in thickness.

In this paper, a polarization-independent absorption of about 99.28% is achieved with $n_s = 1$. However, it is difficult to fabricate such a structure. For practical applications, a substrate should be added below such a structure, which will result in less absorption in graphene than for $n_s = 1$. To enhance the absorption in graphene with a substrate structure, we should increase the number of periods of the SiO$_2$/Si grating layer.

Figure 7
The absorption spectra of the graphene absorber with (*a*) different h_s, (*b*) different h_1 and (*c*) different h_3.

To realise ultra-narrow band absorption, some simpler structures with metallic materials can also be employed (Meng *et al.*, 2014; Li *et al.*, 2014). However, they can only be operated at a single wavelength, *i.e.* they cannot be tuned dynamically over a wide wavelength range, which limits their further application in optoelectronic devices. Although the absorber proposed in this paper is for undoped graphene, where the optical properties of graphene cannot be tuned by changing the Fermi energy, the concept can be applied to the area of doped graphene, which will result in a tunable absorption performance. Therefore, the advantage of using graphene lies in its tunable conductivity. Moreover, the enhancement of absorption in graphene can be employed to develop novel

optoelectronic devices, such as photodetectors, modulators and biosensors.

4. Conclusions

In conclusion, a graphene absorber consisting of a graphene square array resting on a two-dimensional multilayer grating has been designed and investigated. It is shown that total absorption in graphene can be obtained by the critical coupling effect, which combines the effect of guided-mode resonance with the dielectric square array and the photonic band gap with the two-dimensional multilayer grating. The proposed absorber exhibits near-unity polarization-independent absorption at resonance with an ultra-narrow spectrum. Further, the polarization-independent absorption can be tuned simply by changing the geometric parameters. It is believed that the results have potential application in the design of graphene-based photodetectors, thermal emitters and modulators.

Acknowledgements

References

Alaee, R., Farhat, M., Rockstuhl, C. & Lederer, F. (2012). *Opt. Express*, **20**, 28017–28024.

Bao, Q. & Loh, K. P. (2012). *ACS Nano*, **6**, 3677–3694.

Bonaccorso, F., Sun, Z., Hasan, T. & Ferrari, A. C. (2010). *Nat. Photon.* **4**, 611–622.

Bruna, M. & Borini, S. (2009). *Appl. Phys. Lett.* **94**, 031901.

Cai, Y., Zhu, J. & Liu, Q. H. (2015). *Appl. Phys. Lett.* **106**, 043105.

Cheng, H., Chen, S., Yu, P., Duan, X., Xie, B. & Tian, J. (2013). *Appl. Phys. Lett.* **103**, 203112.

Cheng, H., Chen, S., Yu, P., Li, J., Deng, L. & Tian, J. (2013). *Opt. Lett.* **38**, 1567–1569.

Cheng, H., Chen, S., Yu, P., Li, J., Xie, B., Li, Z. & Tian, J. (2013). *Appl. Phys. Lett.* **103**, 223102.

Chern, R. L. & Hong, W. T. (2011). *Opt. Express*, **19**, 8962–8972.

Christensen, J., Manjavacas, A., Thongrattanasiri, S., Koppens, F. H. L. & García de Abajo, F. J. (2012). *ACS Nano*, **6**, 431–440.

Grande, M., Vincenti, M. A., Stomeo, T., Bianco, G. V., de Ceglia, D., Aközbek, N., Petruzzelli, V., Bruno, G., De Vittorio, M., Scalora, M. & D'Orazio, A. (2014). *Opt. Express*, **22**, 31511.

Grigorenko, A. N., Polini, M. & Novoselov, K. S. (2012). *Nat. Photon.* **6**, 749–758.

Hao, J., Zhou, L. & Qiu, M. (2011). *Phys. Rev. B*, **83**, 165107.

Hu, J. H., Huang, Y. Q., Duan, X. F., Wang, Q., Zhang, X., Wang, J. & Ren, X. M. (2014). *Appl. Phys. Lett.* **105**, 221113.

Koppens, F. H. L., Chang, D. E. & García de Abajo, F. J. (2011). *Nano Lett.* **11**, 3370–3377.

Li, J., Yu, P., Cheng, H., Liu, W., Li, Z., Xie, B., Chen, S. & Tian, J. (2016). *Adv. Opt. Mater.* **4**, 91–98.

Li, L. (1997). *J. Opt. Soc. Am. A*, **14**, 2758.

Li, Z., Butun, S. & Aydin, K. (2014). *ACS Nano*, **8**, 8242–8248.

Liu, J. B., Liu, N., Li, J., Li, X. J. & Huang, J. (2016). *Chin. Opt. Lett.* **14**, 052301.

Liu, J., Liu, N., Li, J., Jing Li, X. & Huang, J. (2012). *Appl. Phys. Lett.* **101**, 052104.

Lu, H., Gan, X. T., Mao, D. & Zhao J. L. (2017). *Photon. Res.* **5**, 162.

Mark, K. F., Sfeir, M. Y., Wu, Y., Lui, C. H., Misewich, J. A. & Heinz, T. F. (2008). *Phys. Rev. Lett.* **101**, 196405.

Meng, L., Zhao, D., Ruan, Z., Li, Q., Yang, Y. & Qiu, M. (2014). *Opt. Lett.* **39**, 1137–1140.

Nair, R. R., Blake, P., Grigorenko, A. N., Novoselov, K. S., Booth, T. J., Stauber, T., Peres, N. M. R. & Geim, A. K. (2008). *Science*, **320**, 1308.

Novoselov, K. S., Geim, A. K., Morozov, S. V., Jiang, D., Zhang, Y., Dubonos, S. V., Grigorieva, I. V. & Firsov, A. A. (2004). *Science*, **306**, 666–669.

Piper, J. R. & Fan, S. (2014). *ACS Photon.* **1**, 347–353.

Piper, J. R., Liu, V. & Fan, S. (2014). *Appl. Phys. Lett.* **104**, 251110.

Sensale-Rodriguez, B., Rafique, S., Yan, R., Zhu, M., Protasenko, V., Jena, D., Liu, L. & Xing, H. G. (2013). *Opt. Express*, **21**, 2324–2330.

Thongrattanasiri, S., Koppens, F. H. L. & García de Abajo, F. J. (2012). *Phys. Rev. Lett.* **108**, 047401.

Wang, X., Jiang, X., You, Q., Guo, J., Dai, X. Y. & Xiang, Y. J. (2017). *Photon. Res.* **6**, 536.

Wei, W., Nong, J., Tang, L., Zhang, G., Jiang, X. & Zhu, Y. (2015). *Chin. Opt. Lett.* **13**, 082801.

Wu, L. M., Guo, J., Xu, H., Dai, X. & Xiang, Y. (2016). *Photon. Res.* **4**, 262.

Xia, F. N., Mueller, T., Lin, Y., Valdes-Garcia, A. & Avouris, P. (2009). *Nat. Nanotechnol.* **4**, 839–843.

Xia, F., Yan, H. & Avouris, P. (2013). *Proc. IEEE*, **101**, 1717–1731.

Yang, K., Wang, M., Pu, M., Wu, X., Gao, H., Hu, C. & Luo, X. (2016). *Sci. Rep.* **6**, 23897.

Yang, Y., Shi, Z., Li, J. & Li, Z. (2016). *Photon. Res.* **4**, 65.

Zhang, B. Y., Liu, T., Meng, B., Li, X., Liang, G., Hu, X. & Wang, Q. J. (2013). *Nat. Commun.* **4**, 1811.